



# High-efficiency 11 kW bi-directional on-board charger for EVs

Sang-Youn Lee<sup>1</sup> · Woo-Seok Lee<sup>1</sup> · Jun-Young Lee<sup>1</sup> · Il-Oun Lee<sup>1</sup>

Received: 12 October 2021 / Revised: 9 November 2021 / Accepted: 10 November 2021 / Published online: 10 January 2022  
© The Korean Institute of Power Electronics 2021

## Abstract

This paper presents an 11 kW bi-directional on-board charger (OBC) for electric vehicles with 96% efficiency. The OBC consists of a three-phase two-level AC/DC converter and a CLLLC resonant DC/DC converter with bi-directional power transfer. In order to achieve high efficiency, all the devices in the OBC are implemented using SiC-MOSFETs while the DC-link voltage is designed to track the battery voltage level in both the forward and reverse power modes. The AC/DC converter adopts a DC-link voltage controller that can adapt its control gain according to the status of the DC-link voltage. By adjusting the DC-link voltage level according to the battery voltage, the CLLLC resonant converter always runs at a switching frequency near its resonant frequency. This ensures high-efficiency operation in both the forward and reverse power modes while achieving a full voltage gain. The feasibility of the proposed 11 kW OBC is demonstrated experimentally by constructing a prototype converter with a 3-phase 60 Hz 380 V<sub>AC</sub> input, an 11 kW capacity, and a battery voltage range of 214–413 V<sub>DC</sub>. The prototype OBC achieves a conversion efficiency of over 96% in both the forward and reverse power modes resulting in a power density of over 1.0 kW/liter.

**Keywords** Rapid charger · Electric vehicle · Bi-directional power transfer · High efficiency · 11 kW on-board charger · OBC

## 1 Introduction

In recent years, increasing concerns over global greenhouse gas emissions and fossil fuel depletion have led to an explosion in the demand for electric vehicles (EVs) [1–4]. Due to this demand, there have been many technological improvements in EVs including the adoption of lithium-ion battery packs and the development of electric traction drive systems that use various topologies [5–10]. Today, advanced technology is more pervasive than ever and newer generations of EVs are using higher battery capacities and charging rates to satisfy increasing consumer demands for longer ranges and reduced charging time. To meet these demands, EV charging stations need to supply more power, more quickly than ever before. In addition to the demands that are leading to higher power levels, other trends in the EV charging market are pushing technology on other fronts.

## 2 Higher battery voltage

The EV battery voltage range has moved from 240 to 420 V<sub>DC</sub> to 480–860 V<sub>DC</sub>. As a result, increased vehicle power can be realized at the same current levels and the driving range of an EV can be greatly extended. The cross-section of the wiring harness can be reduced, which results in savings in terms of weight and material costs due to a reduction in the amount of copper [11, 12].

## 3 Bi-directional power flows

The increasing number of EVs has made it possible to use EV batteries as a distributed energy source in a way that allows for grid load balancing when the power from renewable resources has dipped or to accommodate shifts in demand throughout the day. As such, the on-board chargers (OBCs) in EVs must be able to carry bi-directional power flows between a vehicle and the grid [13, 14].

✉ Il-Oun Lee  
leeiloun@mju.ac.kr

<sup>1</sup> Department of Electrical Engineering, Myongji University, Yongin, Republic of Korea

## 4 Increasing power capacity of OBCs

The increase in EV battery capacity for extending the EV driving range has led to the trend of increasing the power capacity of OBCs. In the past, most EVs were equipped with 3.3 kW OBCs. Meanwhile, most present OBCs have a power capacity of either 6.6 kW or 7.2 kW. In the near future, the power capacity of OBCs will move to 11 kW or 22 kW according to the trends of increasing battery capacity and voltage range [15–18].

## 5 Wide-bandgap (WBG) device-based design

Increases in the voltage level or capacity of an EV battery boosts the power rating of OBCs. However, automotive manufactures want OBCs that are the same or smaller in size despite the increase in power capacity. This is to make enough room for loading in cars. This means that a very high power-density design will be required in the development of OBCs in the near future. However, this cannot be achieved with silicon power MOSFETs technology. Wide-bandgap (WBG) power semiconductors like SiC or GaN MOSFETs exceed the performance limits of silicon devices. In addition, they provide a much lower on-resistance, higher breakdown voltage, excellent switching speed, and higher short-term and long-term reliability. Furthermore, they guarantee excellent performance even in critical operating environments. Consequently, the use of WBG devices in OBCs will be necessary to greatly enhance the power density of OBCs [19–21].

Motivated by these trends in EV technology, this paper presents an 11 kW bi-directional on-board charger (OBC) based on SiC-MOSFETs with a high efficiency of over 96% and a power density of over 1.0 kW/liter for electric vehicles. Figure 1 shows the proposed 11 kW OBC, which consists of a three-phase two-level AC/DC converter and a CLLLC DC/DC resonant converter. The 3-phase 2-level AC/DC converter is implemented using an active

six-switch boost-type topology that has advantages such as a simple structure and easy implementation of bi-directional power transmission. However, it has a serious disadvantage when it comes to high voltage stresses. This paper overcomes this by utilizing 1200 V SiC-MOSFETs. A 20 kHz switching frequency is adopted for the AC/DC converter after considering the efficiency and size of both the DC-link capacitors and power inductors. The CLLLC resonant DC/DC converter deals with a great deal of the large circulating current when the operating frequency is far from the resonant frequency. Thus, its conversion-efficiency becomes very poor in these times. To achieve high efficiency over the entire battery voltage range, the DC-link voltage in the proposed OBC is adjusted to track the battery voltage level during the battery charging or generation mode. This algorithm enables the CLLLC resonant converter to always run at a switching frequency near the resonant frequency over the entire battery voltage range in both the forward and reverse power modes. This results in high efficiency for both the forward and reverse power modes while achieving a high-power density for the CLLLC resonant converter. In addition, full voltage-gains covering the entire battery voltage range under certain grid conditions are easily implemented while minimizing the variation in the switching frequency of the CLLLC resonant converter due to variance in the DC-link voltage as dictated by the algorithm. However, a conventional voltage controller with a fixed control gain results in unstable operation in the AC/DC converter due to its variable DC-link voltage. To cope with this problem, the AC/DC converter in the proposed OBC adopts a DC-link voltage controller that adaptively changes its control gain according to the status of the DC-link voltage. The CLLLC resonant converter has a resonant tank that consists of two resonant capacitors, two resonant inductors, and two transformers with a series connection on the primary side and a parallel connection on the secondary side. The resonant tank is designed based on the symmetric design methodology [22, 23] and the turn-ratios of the two transformers are selected to allow the CLLLC resonant converter to run at the resonant frequency with a nominal battery voltage of 330

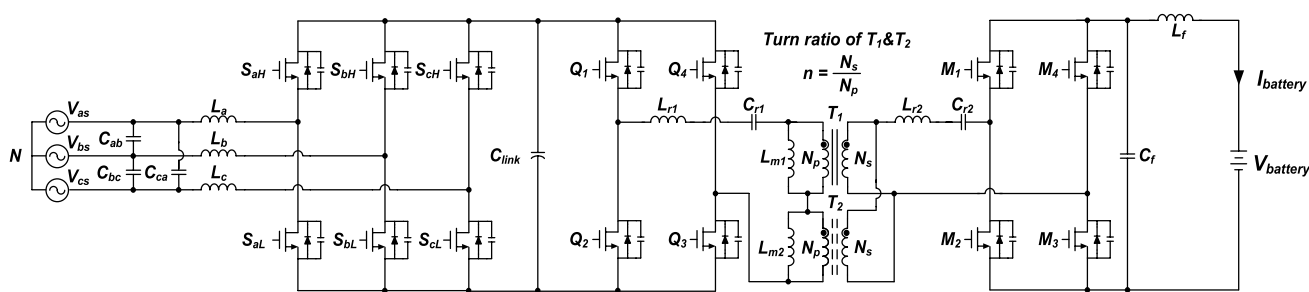


Fig. 1. Proposed topology

$V_{DC}$ . The resonant frequency of the resonant tank in this paper is 140 kHz. This is arrived at by tradeoff between the size of the magnetic components and the amount of switching loss. The characteristic impedances of the resonant tank are designed to minimize the variable range of the switching frequencies. Due to the absence of a large transformer for handling the 11 kW capacity, the CLLLC converter uses two transformers. As a result, a slim design is obtained. The primary and secondary switching devices are implemented with 1200 V and 650 V SiC-MOSFETs, respectively. An inductor-capacitor filter is used in the final stage to attenuate the current ripples in the battery charging current. This paper presents the design philosophy, analysis, and feasibility of the proposed 11 kW OBC.

## 6 AC/DC converter design

The AC/DC converter in the proposed OBC is responsible for power factor correction and DC-link voltage regulation in the charging mode. In the generation mode, it should transfer power from the EV battery to the AC grid while regulating the grid currents in phase with the grid voltages.

Since a single-phase system cannot supply much power over 7.2 kW, OBCs with 11 kW or 22 kW of power generally need three-phase power. The VIENNA topology is very popular for 3-phase AC/DC converters in high-power applications due to the advantages given by its 3-level characteristics, which allow it to select switching devices with a blocking voltage that is half the DC-link voltage [24]. However, the VIENNA topology cannot provide bi-directional power transfer. In this paper, an active six-switch boost-type topology is adopted as the AC/DC converter in the proposed OBC. This is due to the fact that its structure is very simple and bi-directional power transfer is facilitated with the minimum of active switching devices. This active six-switch boost-type topology is known as a three-phase two-level AC/DC converter in some studies [25, 26].

In this paper, the AC/DC converter has a 3-phase 60 Hz 380 V<sub>AC</sub> input grid voltage, an 11 kW capacity, and a 650–900 V<sub>DC</sub> output voltage. The variation between 650 and 900 V<sub>DC</sub> for the DC-link voltage makes it possible to ensure that the CLLLC converter achieves a high efficiency over the entire battery voltage range. The next section deals with the design and specifications of each component in the proposed AC/DC converter.

### 6.1 DC-link voltage range

In this paper, the CLLLC resonant converter, which is used as an isolated DC/DC converter, has the highest efficiency when minimizing circulating current and reducing the turn-off losses of the switch under the same conditions in terms of

switching frequency and resonant frequency. However, since the battery voltage has a wide range of 214–413 V<sub>DC</sub>, at a fixed DC-link voltage, the gain of the CLLLC resonant converter must be changed significantly for charging. A variable wide switching frequency range is required to do this. These large changes in the gain lead to a rapid deterioration of the efficiency due to increases in the circulating current and turn-off loss. In this paper, the CLLLC resonant converter is designed to always operate near the resonant frequency by varying the DC-link voltage according to the battery voltage. The variable DC-link voltage range is selected in consideration of the power factor control performance and efficiency optimization at the nominal battery voltage as follows.

The AC/DC converter must operate in the linear modulation domain so that it can act as a power factor correction circuit. When the space vector PWM (SVPWM) method is used, the voltage modulation index (MI) is operated in a linear modulation range up to 1.15. The formula for the MI is given in Eq. (1).

$$MI = \frac{V_{ac\_peak}}{V_{DC\_link}/2}. \quad (1)$$

According to Eq. (1), the minimum DC-link voltage for the AC/DC converter to operate in the linear modulation region under a grid voltage of 380 V<sub>AC</sub> is 540 V<sub>DC</sub>. The minimum DC-link voltage after considering a 10% error in the grid voltage becomes greater than 600 V<sub>DC</sub>. When considering the conduction loss generated by the AC/DC converter, the minimum DC-link voltage was finally selected as 650 V<sub>DC</sub>. In addition, since 1200 V SiC-MOSFETs are used for the AC/DC converters, the maximum DC-link voltage was selected to be 900 V<sub>DC</sub> in consideration of an appropriate voltage margin. Equation (2) shows the range of the applicable DC-link voltage.

$$650[V] \leq V_{DC\_link} \leq 900[V]. \quad (2)$$

When the CLLLC resonant converter operates at its resonant frequency, the gain equation between the DC-link voltage and the battery voltage can be expressed as follows:

$$\frac{V_{battery}}{V_{DC\_link}} = \frac{N_S}{2N_P} = \frac{1}{2n}. \quad (3)$$

According to Eq. (3), when the CLLLC resonant converter is designed to operate at its resonant frequency over the entire battery voltage range of 214–413 V<sub>DC</sub>, if the turn-ratio  $n$  is designed to be 1.5, the maximum DC-link voltage becomes 1200 V or higher. This makes it very difficult to select an AC/DC converter element. It becomes practically impossible to operate the CLLLC resonant converter with a high turn-ratio over the entire battery voltage range. The nominal voltage of the battery used in this study is 330 V,

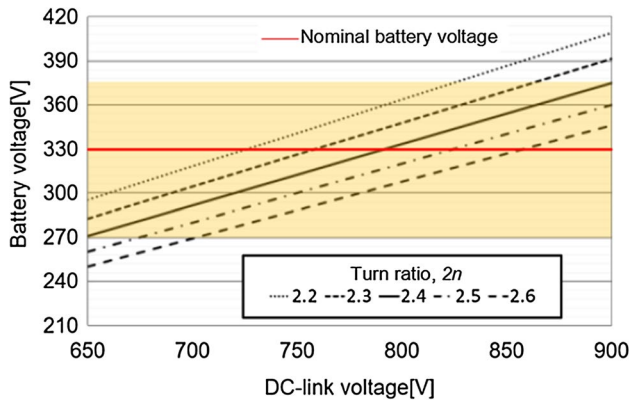


**Fig. 2** Battery voltage range according to the available DC-link voltage and turn-ratio

a high efficiency of 95% or more is required at this voltage. Figure 2 shows the results of analyzing the battery voltage range when the CLLLC resonant converter operates at its resonant frequency according to various turn-ratios under the conditions set out in Eq. (2). Looking at Fig. 2, it can be seen that when the turn-ratio  $n$  is 1.2, a high efficiency in the wide battery voltage range that includes the nominal voltage is guaranteed.

Figure 3 shows the DC-link voltage variable range according to the battery voltage when the turn-ratio  $n$  is 1.2. At 270–375  $V_{DC}$ , including the nominal voltage of the battery, the DC-link voltage changes to 650–900  $V_{DC}$ . Thus, the CLLLC resonant converter can operate at the resonant frequency. When  $V_{DC}$  is below 270 or above 350, the DC-link voltage is fixed at 650  $V_{DC}$  or 900  $V_{DC}$ , and the CLLLC resonant converter allows the battery to be charged with a variable frequency.

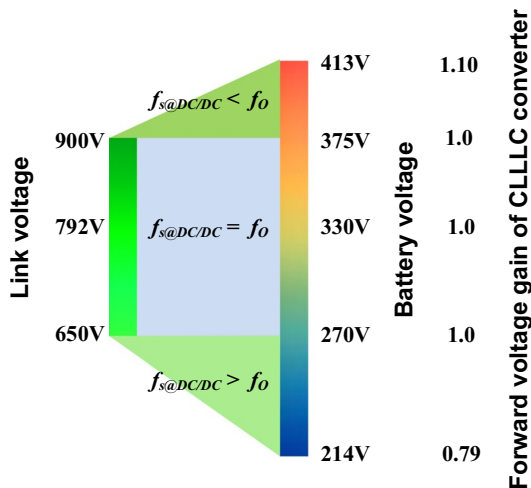


**Fig. 3** DC-link voltage range for the 11 kW OBC

## 6.2 Switching frequency and passive components

The switching frequency is optimized by analyzing the efficiency of the AC/DC converter and the size of the passive elements used.

The conduction, capacitive, and switching losses generated in the switch of the AC/DC converter are expressed in Eq. (4).

$$P_{SW@AC/DC} = 6[(E_{on} + E_{off})f_{s@AC/DC} + \frac{1}{2}C_{oss}V_{DC\_link}^2f_{s@AC/DC} + R_{DS}I_{rms@S_{aH\sim cL}}^2]. \quad (4)$$

The required size of the inductor is given by Eq. (5).

$$L = \frac{V_{ac\_peak}}{\Delta i_{L\_max} \times f_{s@AC/DC}} (0.5 - \frac{V_{ac\_peak}}{2V_{DC}}). \quad (5)$$

The size of the DC-link capacitor is designed based on Eq. (6).

$$C_{link} = \frac{P_{O(max)}}{4 \times V_{DC\_link} \times \Delta V_{DC\_link} \times f_{s@AC/DC}}. \quad (6)$$

Using Eqs. (4), (5), and (6), it is possible to find the expected efficiency, required inductance, and required capacitance of the AC/DC converter given the conditions of a switching frequency under 60 Hz, 380  $V_{AC}$ , 900  $V_{DC\_link}$ , and 11 kW capacity. How these quantities vary in relation to each other is shown in Fig. 4. Considering the achievable efficiency of the AC/DC converter and the size of the passive element, the AC/DC converter is driven at 20 kHz.

From Fig. 4, it can be seen that the inductor  $L_a$  (or  $L_b$  or  $L_c$ ) for the AC/DC converter, when applying the selected 20 kHz switching frequency and a maximum current ripple of 2.5 A, should be 2 mH. The maximum current flowing through the inductor can be obtained as follows:

$$I_{rms@L_{abc}} = \frac{\sqrt{3}P_{O(max)}}{3V_{AC(rms)}} = \frac{\sqrt{3} \times 11000}{3 \times 380} = 16.7[A];$$

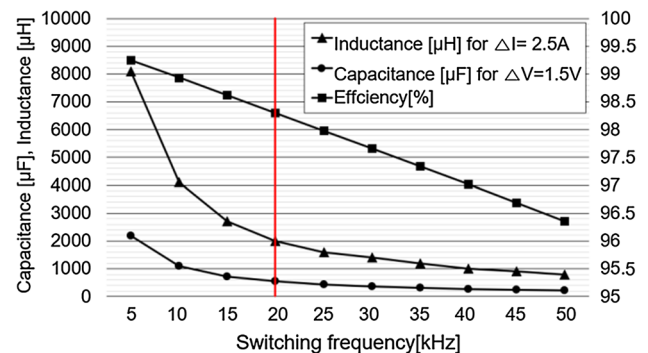


**Fig. 4** AC/DC converter analysis according to the switching frequency

$$\begin{aligned}
 I_{peak@L_{abc}} &= \sqrt{2}I_{rms@L_{abc}} + \frac{\Delta I_{ripple}}{2} = \sqrt{2}I_{rms@L_{abc}} + \frac{2.5}{2}. \\
 &= 24.9[\text{A}]
 \end{aligned} \quad (7)$$

Then, the size of the core is obtained from Eq. (8).

$$LI^2 = 2 \times 24.9^2 = 1240[\text{mHA}^2]. \quad (8)$$

From the result of Eq. (8), a CH740060 high flux powder core is selected. The number of turns to meet an inductance of 2 mH is calculated as 99 turns.

The link-capacitor of the AC/DC converter is designed based on a selected switching frequency of 20 kHz and a maximum voltage ripple of 1.5 V. The appropriate capacitance, where the current flows the most, based on 790 V<sub>DC\_link</sub> and 11 kW capacity conditions, is given in Eq. (9).

$$C_{link} > 520 [\mu\text{F}]. \quad (9)$$

As such, in this paper, a 550  $\mu\text{F}$  link capacitor with 1200 V<sub>DC</sub> breakdown voltage is used in 2 series and 5 parallel capacitors with a 220  $\mu\text{F}$  capacitance and a 600 V<sub>DC</sub> withstand voltage.

### 6.3 Power semiconductors

The power semiconductor devices used in the AC/DC converter are selected based on their voltage stress, current stress, and power loss characteristics. The maximum voltage, peak current stress, and root-mean-square (rms) current stress parameters that dictate device selection are obtained from Eqs. (10) and (11).

$$\begin{aligned}
 I_{peak@S_{aH\sim cL}} &= \frac{P_{O(max)}}{\sqrt{3}V_{AC\_rms}} \times \sqrt{2} = 26.63[\text{A}] \text{ and} \\
 I_{rms@S_{aH\sim cL}} &= \frac{I_{peak@S_{aH\sim cL}}}{4} = 5.9[\text{A}];
 \end{aligned} \quad (10)$$

$$V_{peak@S_{aH\sim cL}} = V_{DC\_link(max)} = 900[\text{V}]. \quad (11)$$

An IMW120R045M1 SiC-MOSFET is selected as the switching devices by considering the electrical stresses generated in the switch.

## 7 CLLC resonant converter design

Topologies commonly used as isolated DC/DC converters for OBCs include phase-shifted full-bridge (PSFB) converters and LLC resonant converters. Bi-directional operation is made possible by applying the rectification stage of a PSFB converter as a synchronous rectifier. However, if the output voltage is high, like for a battery charger, the snubber loss is greatly increased due to a serious voltage rigging problem at

the rectifier stage. A 1200 V class power semiconductor can be applied as a synchronous rectifier switch in consideration of this high voltage rigging issue. However, doing this leads to increased material costs, low bi-directional power-conversion efficiency, and EMI issues [27]. LLC resonant converters are also capable of bi-directional power transmission by applying a synchronous rectifier instead of a diode rectifier. Unlike the PSFB converter, since voltage rigging does not occur at the rectifier, it can be implemented with a 650 V class power semiconductor. In addition, since the zero-voltage-switching (ZVS) operation and the zero-current-switching (ZCS) operation are achieved in both the full-load area and in bi-directional power transfer, this approach has the advantage of achieving a high efficiency. With this implementation, in the forward power transfer mode, the voltage gain has both buck and boost characteristics. However, in the reverse power transfer mode, it only has buck characteristics with voltage gains lower than one. As such, it is known that LLC resonant converters are not suitable for applications that require both buck and boost features in both directions, such as bi-directional battery charger applications [28, 29].

In this paper, a CLLLC resonant converter, which is capable of bi-directional operation and has the advantage of achieving a high efficiency through ZVS and ZCS operations, is used as an isolated DC/DC converter. The CLLLC resonant converter consists of a primary-side full-bridge inverter unit, a primary-side resonance tank, a transformer, a secondary-side resonance tank, and a secondary-side full-bridge rectification unit. The resonant tanks are on both the primary and secondary sides of the transformer giving it both buck and boost voltage gain characteristics regardless of the power flow, which makes it suitable for bi-directional battery charger applications. The CLLLC resonant converter applied in this paper has a 650–900 V<sub>DC</sub> input, an 11 kW power capacity, and battery voltage specifications of 214–413 V<sub>DC</sub>. This section describes the optimization of the bi-directional CLLLC resonant converter according to the given specifications.

### 7.1 Resonant frequency

The CLLLC resonant converter basically controls the output by varying the switching frequency around the resonant frequency. Therefore, it is important to select the resonant frequency of the CLLLC resonant converter.

As described in the previous chapter, to optimize the efficiency of the CLLLC resonant converter during battery charging or generation, the switching frequency must operate at a resonant frequency in the 270–375 V<sub>DC</sub> region of battery voltage, where a maximum power of 11 kW is provided, as shown in Fig. 3. Therefore, it is necessary to optimize the resonant frequency  $f_o$  by analyzing the CLLLC resonant converter efficiency and the main transformer size



in the battery voltage region of 270–375 V<sub>DC</sub> that provides the maximum power.

In the CLLLC resonant converter, capacitive losses and turn-on switching losses do not occur due to the ZVS operation in the primary switch. However, turn-off switching losses and conduction losses are generated. This can be expressed as in Eq. (12).

$$P_{PRI.SW@DC/DC} = 4(E_{off@pri}f_o + R_{DS@pri}I_{rms@Q_{pri}}^2). \quad (12)$$

Here,  $E_{off@pri}$  is the turn-off energy of the primary switch, and  $R_{DS@pri}$  is the on-state resistance.  $I_{rms@Q_{pri}}$  is the effective current flowing through each of the primary switches, which is calculated from Eq. (13).

$$I_{rms@Q_{pri}} = \frac{I_{peak@L_{r1}}}{2} = \frac{\pi P_{O(max)}}{8nV_{battery}}. \quad (13)$$

The secondary switch only has conduction losses due to the operation of the synchronous rectifier, which is expressed in Eq. (14).

$$P_{SEC.SW@DC/DC} = 4R_{DS@sec}I_{rms@M_{sec}}^2. \quad (14)$$

where  $R_{DS@sec}$  is the on-state resistance of the secondary switch.  $I_{rms@M_{sec}}$  is the effective current flowing through each of the secondary switches, which is calculated from Eq. (15).

$$I_{rms@M_{sec}} = \frac{I_{peak@L_{r2}}}{2} = \frac{\pi P_{O(max)}}{4V_{battery}}. \quad (15)$$

The high-frequency transformer is manufactured using a ferrite core. The size of the magnetic element is dictated by the product of the window area  $W_a$  and the cross-sectional area  $A_c$  of the core used as in Eq. (16).  $B_m$  is the maximum magnetic flux-density in the Tesla, and 0.13 T is selected to achieve small core losses.  $J$  is the current-density, which is selected to be 450 A/cm<sup>2</sup> to maintain the coil temperature around 70 °C in a room temperature environment.  $P_{O(max)}$  is set to the maximum power of 11 kW.

$$A_{P(T_1 \text{ or } T_2)} = W_a A_c \geq \left[ \frac{0.5P_{O(max)} \times 10^4}{0.66 \times B_m \times f_o \times J} \right]^{4/3} [\text{cm}^4]. \quad (16)$$

The ferrite core for the transformers uses a PM16 material with core losses of 264 mW/cm<sup>3</sup> at 100 kHz, 0.2 T, and 80 °C. The transformer core and copper losses are given in Eq. (17).

$$P_{core@T_1 \text{ or } T_2} = \frac{264 \times \left(\frac{f_o}{10^5}\right)^{1.3} \times \left(\frac{B_m}{0.2}\right)^{2.5}}{4850 \times 1000} \times W_{weight} \text{ and} \\ P_{copper@T_1 \text{ or } T_2} = R_{copper@pri}I_{rms@pri}^2 + R_{copper@sec}I_{rms@sec}^2. \quad (17)$$

In Eq. (17),  $W_{weight}$  is the weight of the core used to manufacture the transformer,  $R_{copper@pri}$  is the primary winding resistance, and  $R_{copper@sec}$  is the secondary winding resistance.  $I_{rms@pri}$  is the current flowing through the primary side of the transformer, and  $I_{rms@sec}$  is the current flowing through the secondary side as calculated by Eq. (18).

$$I_{rms@pri} = \sqrt{(I_{rms@sec} \times \frac{N_s}{N_p})^2 + \frac{1}{12} \left( \frac{\frac{2N_p}{N_s} V_{battery}}{2L_m f_o} \right)^2} \text{ and} \\ I_{rms@sec} = \frac{\pi P_{O(max)}}{4\sqrt{2}V_{battery}}. \quad (18)$$

Figure 5 shows the expected efficiency for a given transformer size derived from Eqs. (13), (15), (17), and (18) according to the resonant frequency of the CLLLC resonant converter under 792 V<sub>DC\_link</sub>, 330 V<sub>battery</sub>, and 11 kW conditions. Looking at the analysis in Fig. 5, it can be seen that a resonance frequency of 140 kHz is the most optimal in terms of the achieved high power-density and high efficiency.

## 7.2 Main transformer

Given an 11 kW CLLLC resonant converter, designing a single transformer in the 11 kW capacity class results in a problem in terms of the height and size of the transformer becoming very large. Thus, to achieve a high power-density OBC in this paper, two 5.5 kW class transformers are designed and manufactured to work together to give a compact 11 kW OBC. As shown in Fig. 1, the primary windings are connected in series and the secondary windings are connected in parallel so the power flowing through the two transformers is balanced. The turn-ratio of each transformer is determined to be 1.2 in part A of the previous section.

Through the analysis in Fig. 5, the optimum size of the ferrite core used to fabricate the transformers  $T_1$  and  $T_2$  is given in Eq. (19).

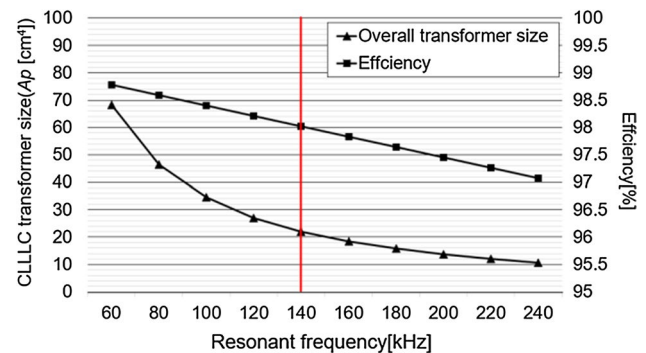


Fig. 5 CLLLC resonant converter analysis according to the resonant frequency

$$A_{P(T_1 \text{ or } T_2)} = W_a A_C \geq 22.0 [\text{cm}^4]. \quad (19)$$

The magnetic element that satisfies the result in Eq. (19) is PQ6145, as is shown in Fig. 6. The window area  $W_a$  of the PQ6145 is  $4.5 \text{ cm}^2$ , the cross-sectional area  $A_C$  is  $4.9 \text{ cm}^2$ , while that of  $A_P$  is  $22.0 \text{ cm}^4$ . In addition, the weight is 258 g. 12 turns are chosen for the primary side according to Faraday's law. Then, the turn-ratio determines the number of turns on the secondary side to be 10.

The magnetizing inductances of  $T_1$  and  $T_2$  are chosen in consideration of the ZVS condition of the primary switch, which is described in Eq. (20).

$$L_m = L_{m1} + L_{m2} \leq \frac{T_{dead}}{16 \left( C_{oss@pri} + \frac{C_{oss@sec}}{4n^2} \right) f_O} = 230 [\mu\text{H}]. \quad (20)$$

In Eq. (20),  $C_{oss@pri}$  is the output-junction capacitance of the primary switch, and  $C_{oss@sec}$  is the output-junction capacitance of the secondary switch. Given that the primary switch is a SCTWA50N120 SiC-MOSFET, the secondary switch is a SCT3030AL SiC-MOSFET, and  $T_{dead}$  is 200 nsec, the total magnetizing inductance  $L_m$  for the ZVS operation must be less than 230  $\mu\text{H}$ . Thus, the magnetizing inductance of each transformer should be less than 115  $\mu\text{H}$ .

The primary and secondary windings use litz wires with 0.1 mm/300 strands and 0.1 mm/600 strands, respectively. These values are chosen in consideration of the current stress calculated in Eq. (18).

### 7.3 Voltage gain analysis and resonant parameter design

The resonant parameters of the CLLLC resonant converter in this paper are designed based on the symmetric design methodology [26, 27]. Then, according to the principle of fundamental harmonic approximation (FHA), the resonant tank is equalized as shown in Fig. 7 during charging, and as shown in Fig. 8 during generation. All of the parameters in Fig. 7 and Fig. 8 are given below:

$$L_m = L_{m1} + L_{m2}, L_r = L_{r1}, C_r = C_{r1}, \gamma L_r = 4n^2 L_{r2}, \\ \frac{C_r}{\gamma} = \frac{C_{r2}}{4n^2}, R_{C(ac)} = \frac{32n^2}{\pi^2} \frac{V_{battery}^2}{P_O}, \text{ and}$$

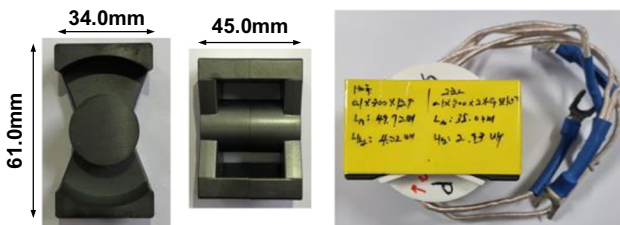


Fig. 6 Used magnetic core and manufactured 5.5 kW transformer

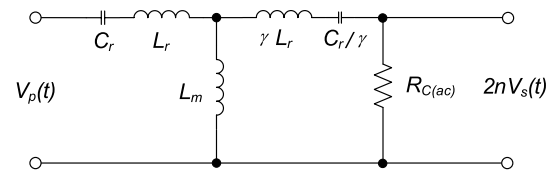


Fig. 7 Charging mode equivalent circuit model of the CLLLC resonant converter

$$R_{G(ac)} = \frac{8}{\pi^2} \frac{V_{DC\_link}^2}{P_O}. \quad (21)$$

The voltage gain of the CLLLC resonant converter during charging, as shown in Fig. 7, is obtained using Eq. (22).

$$\frac{2nV_s(t)}{V_p(t)} = M_{@charging} = \frac{1}{\sqrt{\alpha_{@charging}^2 + \beta_{@charging}^2}}, \quad (22)$$

where  $\alpha_{@charging} = \frac{1}{k} \left( 1 - \frac{1}{f_n^2} \right) + 1$  and

$$\beta_{@charging} = Q_C \left[ f_n \left( 1 + \gamma + \frac{\gamma}{k} \right) - \frac{1}{f_n} \left( 1 + \gamma + \frac{2\gamma}{k} \right) + \frac{\gamma}{kf_n^3} \right].$$

The voltage gain of the CLLLC resonant converter during generation, as shown in Fig. 8, is obtained using Eq. (23).

$$\frac{V_p(t)}{2nV_s(t)} = M_{@generation} = \frac{1}{\sqrt{\alpha_{@generation}^2 + \beta_{@generation}^2}}, \quad (23)$$

where  $\alpha_{@generation} = \frac{\gamma}{k} \left( 1 - \frac{1}{f_n^2} \right) + 1$  and

$$\beta_{@generation} = Q_G \left[ f_n \left( 1 + \gamma + \frac{\gamma}{k} \right) - \frac{1}{f_n} \left( 1 + \gamma + \frac{2\gamma}{k} \right) + \frac{\gamma}{kf_n^3} \right].$$

In Eqs. (23) and (24), each of the variables is defined as follows.  $f_O$  is the resonance frequency, which is determined by  $L_r$  and  $C_r$ . Meanwhile,  $Z_O$  is the characteristic impedance of the resonance tank.

$Q_C$  and  $Q_G$  are the quality factors during charging and generation, respectively.  $k$  is the ratio of the transformer magnetizing inductance  $L_m$  and the resonant inductance  $L_r$ . In addition,  $f_n$  represents the normalized switching frequency.

$$k = \frac{L_m}{L_r}, Q_C = \frac{Z_O}{R_{C(ac)}}, Q_G = \frac{Z_O}{R_{G(ac)}}, f_O = \frac{1}{2\pi\sqrt{L_r C_r}},$$

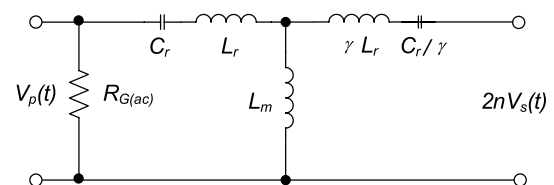


Fig. 8 Generation mode equivalent circuit model of the CLLLC resonant converter

$$Z_O = \sqrt{\frac{L_r}{C_r}}, \text{ and } f_n = \frac{f_{SW@DC/DC}}{f_o}. \quad (24)$$

From Eqs. (22) and (23), it can be seen that the voltage gain during charging or generation is affected by  $\gamma$ ,  $k$ , and the quality factors. Therefore,  $\gamma$ ,  $k$ , and the quality factors should be determined before choosing the other resonant parameters.

In the charging and generation modes of the CLLLC resonant converter, the voltage gain region, where the switching frequency should be modulated, is as in Eq. (25) from Fig. 3.

$$0.79 \leq M_{@charging} \leq 1.10$$

$$0.91 \leq M_{@generation} \leq 1.27 \quad (25)$$

Figure 9a shows the charging mode voltage gain according to the “ $\gamma$  factor”. As can be seen from the graph, the  $k$  factor should be selected first since the influence the  $\gamma$  factor has in the charging mode is insignificant. Figure 9b shows the voltage gain change according to the  $k$  factor given that the “ $\gamma$  factor” is 1, where the magnetizing inductance and resonance frequency are as selected in the previous part.

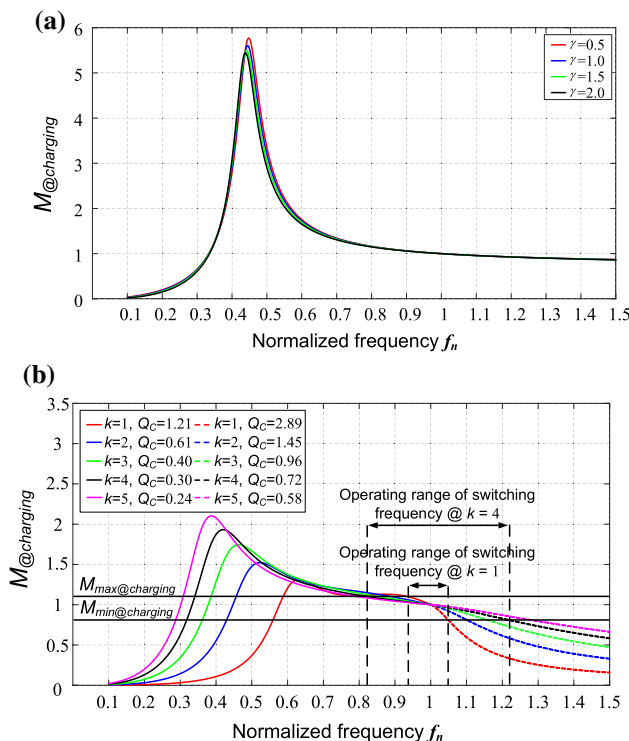


**Fig. 9** Voltage gain,  $M_{@charging}$  in the charging mode: **a**  $M_{@charging}$  according to different  $\gamma$  values with  $Q_C=0.1$  and  $k=4$ ; **b**  $M_{@charging}$  according to different  $k$  values with  $\gamma=1$ ,  $L_m=100 \mu\text{H}$ , and  $f_o=140 \text{ kHz}$

Here,  $Q_C$  is based on the  $900 \text{ V}_{\text{DC-link}}$ ,  $413 \text{ V}_{\text{battery}}$ , and  $11 \text{ kW}$  conditions in the  $f_n$  range of 1 or less from Eqs. (22) and (25), and calculated based on the  $650 \text{ V}_{\text{DC-link}}$ ,  $214 \text{ V}_{\text{battery}}$ , and  $7 \text{ kW}$  conditions in the  $f_n$  range of 1 or more. Considering the variable switching frequency range, the size of the resonant inductors, and the maximum voltage gain, the  $k$  factor is selected to be 4. Figure 10 shows the generation mode voltage gain according to the  $\gamma$  factor under the selected  $k$  factor, magnetizing inductance, and resonance frequency conditions. In this generation mode voltage gain analysis,  $Q_G$  is calculated based on the  $650 \text{ V}_{\text{DC-link}}$ ,  $214 \text{ V}_{\text{battery}}$ , and  $7 \text{ kW}$  conditions, from Eqs. (22) and (25) when  $f_n$  is 1 or less, and it is calculated based on the  $900 \text{ V}_{\text{DC-link}}$ ,  $413 \text{ V}_{\text{battery}}$ , and  $11 \text{ kW}$  condition in the  $f_n$  range of 1 or more. In consideration of the variable switching frequency range and the maximum voltage gain,  $\gamma$  is selected to be 1.2. Finally,  $\gamma$ ,  $k$ ,  $L_m$ , and  $f_o$  are selected as shown in Table 1. Then, the resonant parameters for the CLLLC resonant converter are designed around these factors.

## 7.4 Power semiconductors

The electrical stresses of the primary power semiconductor switch of the CLLLC resonant converter are given in Eq. (26).

$$I_{\text{peak}@Q_{pri}} = \frac{\pi P_{O(\text{max})}}{4nV_{\text{battery}}} = 21.8[\text{A}],$$

$$I_{\text{rms}@Q_{pri}} = \frac{I_{\text{peak}@Q_{pri}}}{2} = 10.9[\text{A}], \text{ and}$$

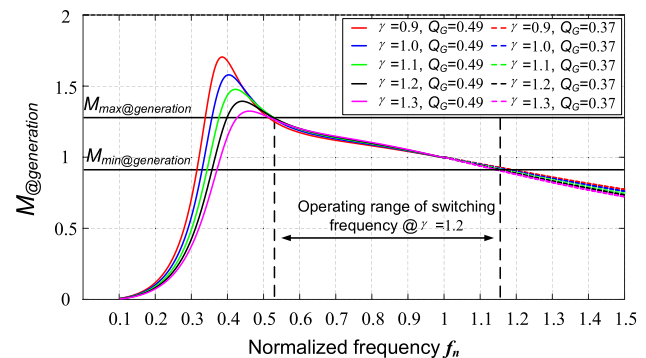


**Fig. 10** Voltage gain,  $M_{@generation}$  in the generation mode according to different  $\gamma$  values with  $k=4$ ,  $L_m=100 \mu\text{H}$ , and  $f_o=140 \text{ kHz}$

**Table 1** Resonant parameters for the CLLLC resonant converter

Parameters	Value	Parameters	Value
$\gamma$	1.2	$L_{r1}$	25[ $\mu\text{H}$ ]
$k$	4	$L_{r2}$	5.2[ $\mu\text{H}$ ]
$f_o$	140[kHz]	$C_{r1}$	52[nF]
$L_m$	100[ $\mu\text{H}$ ]	$C_{r2}$	250[nF]



$$V_{peak@Q_{pri}} = V_{DC\_link(max)} = 900[V]. \quad (26)$$

A SCTWA50N120 SiC-MOSFET is selected as the switching element in consideration of the electrical stresses, and it is implemented using 2 devices in parallel considering the heat generation based on the loss analysis.

Equation (27) shows the electrical stresses for the design of the secondary switch.

$$\begin{aligned} I_{peak@M_{sec}} &= \frac{\pi P_{O(max)}}{2V_{battery}} = 52.4[A], \\ I_{rms@M_{sec}} &= \frac{I_{peak@M_{sec}}}{2} = 26.2[A], \\ V_{peak@M_{sec}} &= V_{battery(max)} = 413[V]. \end{aligned} \quad (27)$$

By considering the results of Eq. (28), a SCT3030AL SiC-MOSFET is chosen and two devices are implemented in parallel due to the expected thermal stress.

## 7.5 Control algorithm

Figure 11 shows the charging mode control algorithm of the proposed OBC. The AC/DC converter provides the DC-link voltage through the DC-link voltage control. The DC-link voltage reference value is set as follows so that the CLLLC resonant converter can operate near its resonant frequency.

$$V_{DC\_link\_ref} = V_{battery} \times 2n, \text{ where } n = 1.2. \quad (28)$$

An adaptive voltage PI controller that adaptively changes the gain of the controller according to the DC-link voltage

is applied so that the fluctuation of the DC-link voltage does not affect the control performance of the AC/DC converter.

The CLLLC resonant converter charges the battery through constant-current (CC) and constant-power (CP) control. In addition, it gradually charges the battery through constant-voltage (CV) control when the battery voltage reaches the target voltage of 413 V<sub>DC</sub>. At this time, to reduce any conduction losses, the secondary side of the CLLLC resonant converter is operated as a synchronous rectifier.

Figure 12 shows the generation control algorithm of the proposed OBC topology. In the generation mode, the CLLLC resonant converter performs DC-link voltage control, and generates a DC-link voltage reference value according to Eq. (28), which allows it to operate near the resonant frequency. The generation active power controller receives a power command ( $P_{o\_cmd}$ ) from the host controller to control the amount of discharged power using current control at the DC-AC inverter stage. Other control algorithms work in a similar way to the charging mode.

## 8 Experimental results

To verify the performance of the proposed OBC topology, a bi-directional OBC prototype was implemented with the following specifications:

- Grid voltage:  $V_{AC(rms)} = 380$  V<sub>AC</sub>
- DC-link voltage:  $V_{DC\_link} = 650\text{--}900$  V<sub>DC</sub>
- Battery voltage:  $V_{battery} = 214\text{--}413$  V<sub>DC</sub>

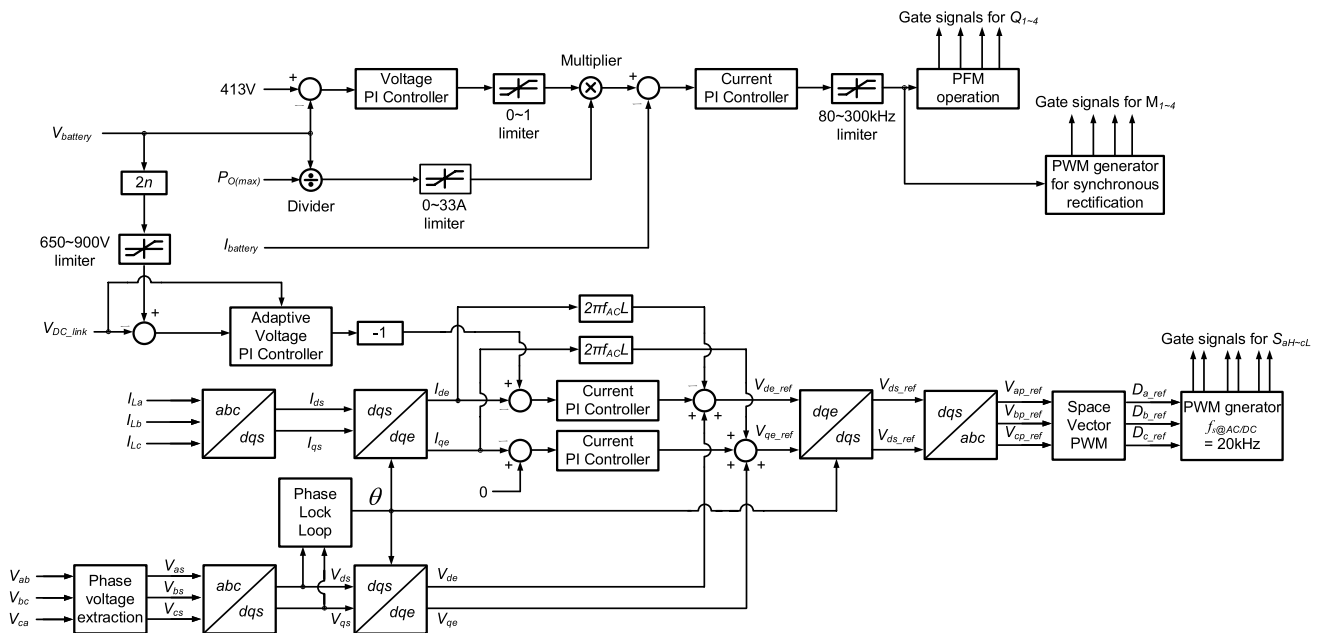
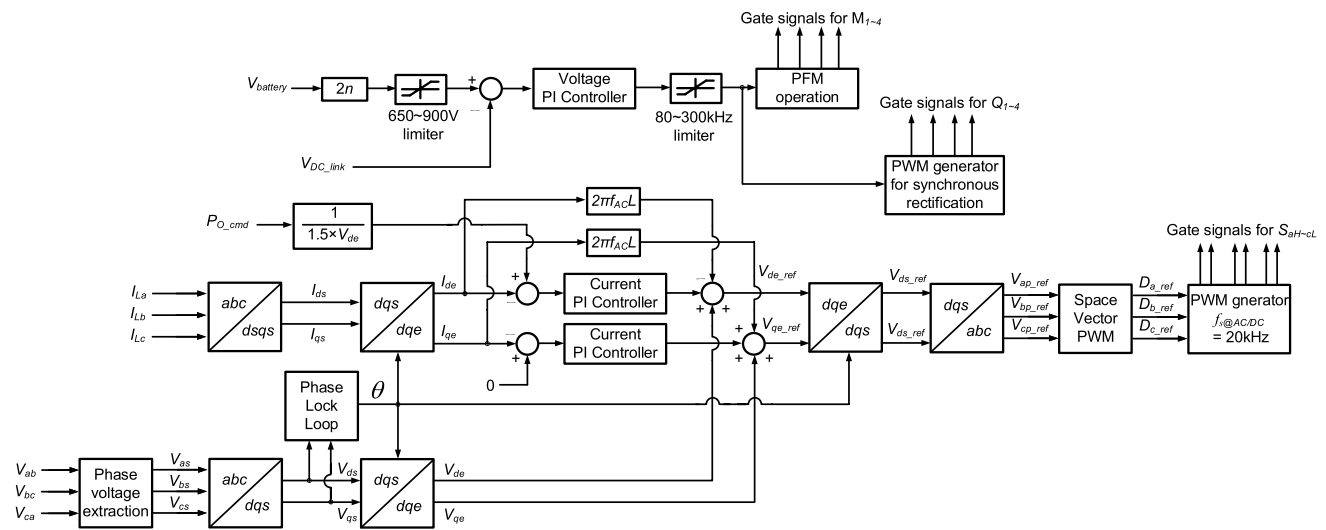


Fig. 11 Control algorithm for the charging mode of the proposed OBC topology in the steady state



**Fig. 12** Control algorithm for the generation mode of the proposed OBC topology in the steady state

**Table 2** Component list

Components	Parameters
Input filter capacitor ( $C_{ab}$ , $C_{bc}$ , $C_{ca}$ )	3.3 $\mu$ F
AC/DC inductor ( $L_a$ , $L_b$ , $L_c$ )	2 mH
AC/DC switches ( $S_{aH-cl}$ )	IMW120R045M1
Link capacitors ( $C_{link}$ )	550 $\mu$ F
Primary switches ( $Q_{1-4}$ )	SCTWA50N120
Primary resonant inductor ( $L_{r1}$ )	20 $\mu$ H
Primary resonant capacitor ( $C_{r1}$ )	55 nF
Transformers ( $T_1$ , $T_2$ )	$L_m$ : 49.7 $\mu$ H $L_{kg}$ : 4.0 $\mu$ H
Secondary resonant inductor ( $L_{r2}$ )	5.46 $\mu$ H
Secondary resonant capacitor ( $C_{r2}$ )	300 nF
Secondary switches ( $M_{1-4}$ )	SCT3030AL
Output filter capacitor ( $C_r$ )	2.2 $\mu$ F
Output filter inductor ( $L_r$ )	50 $\mu$ H

- Maximum battery current:  $I_{battery(max)} = 33$  A
- Maximum output power:  $P_{O(max)} = 11$  kW

Table 2 summarizes the design parameters used for the prototype. All of the control algorithms are implemented using a TMS320F28335. Experimental results come from charging and generation tests using an actual AC system and an electric vehicle battery.

Figures 13 and 14 show experimental waveforms in the charging mode under the conditions of a nominal battery voltage of 330 V and a maximum voltage of 413 V. Figures 13a and 14a show grid currents during the charging mode operation. From these waveforms, it can be seen that the grid current control is well carried out. Figure 13b shows that the switching frequency of the CLLLC resonant converter is 135 kHz under the nominal voltage of the charge mode battery and that it is operating in the

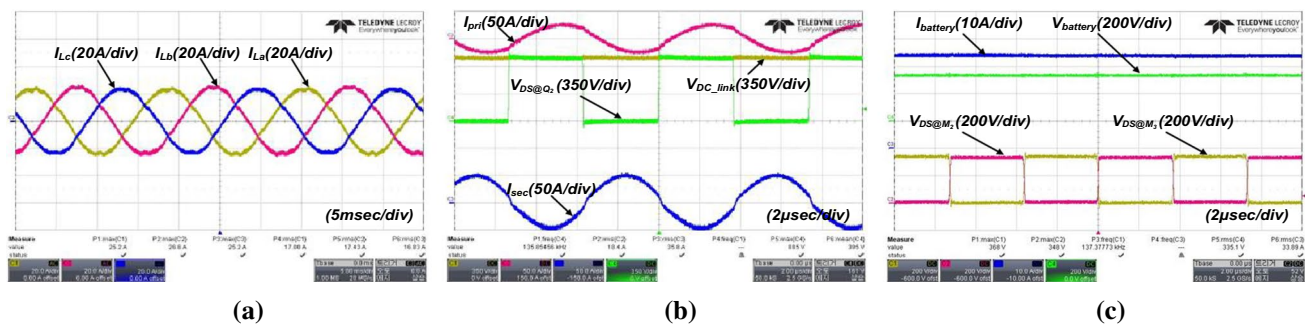


**Fig. 13** Key waveforms in the charging mode with a nominal battery voltage of 330 V: **a** input currents; **b** resonant currents, primary switch voltage, and DC-link voltage; **c** battery current, battery voltage, and secondary switch voltages

resonant frequency range as designed in the previous section. Figure 14b shows results from testing with the maximum battery voltage in the charge mode. It can be seen that the CLLC converter switching frequency is adjusted to 120 kHz, which is lower than the resonant frequency. From Figs. 13b and 14b, it can be seen that ZVS operation is achieved through the voltage waveform across the primary-side switch and the primary-side resonant current waveform. Figures 13c and 14c show battery charging current, battery voltage, and secondary switch voltage waveforms. It can be

seen that the proposed OBC prototype does a good job of charging the real battery in an EV.

Figures 15 and 16 show test waveforms of the generation mode under a nominal battery voltage of 330 V and a maximum voltage of 413 V. Based on the theoretical analysis and design, the CLLC converter switching frequency is near the resonant frequency at a nominal battery voltage of 330 V and larger than the resonant frequency under a maximum battery voltage of 413 V. The switching frequency in Fig. 15b is lower than the resonance frequency. However, it operates in the resonance frequency domain in Fig. 16b.

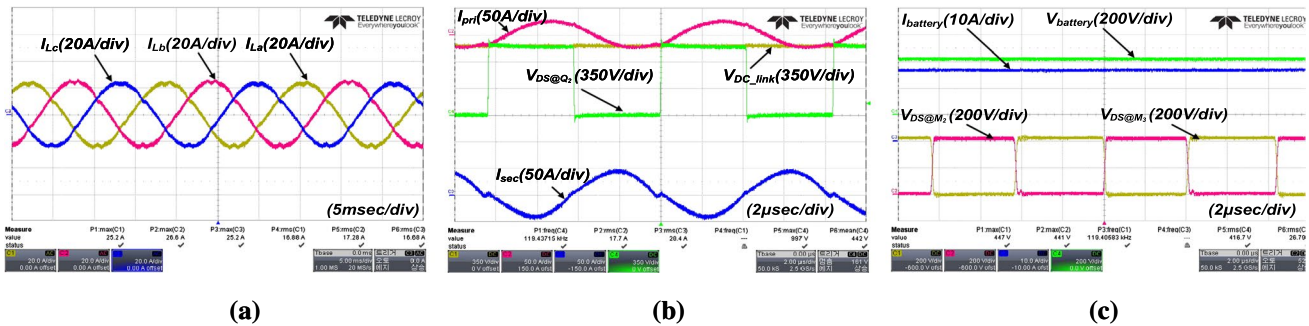


**Fig. 14** Key waveforms in the charging mode with a nominal battery voltage of 413 V: **a** input currents; **b** resonant currents, primary switch voltage, and DC-link voltage; **c** battery current, battery voltage, and secondary switch voltages

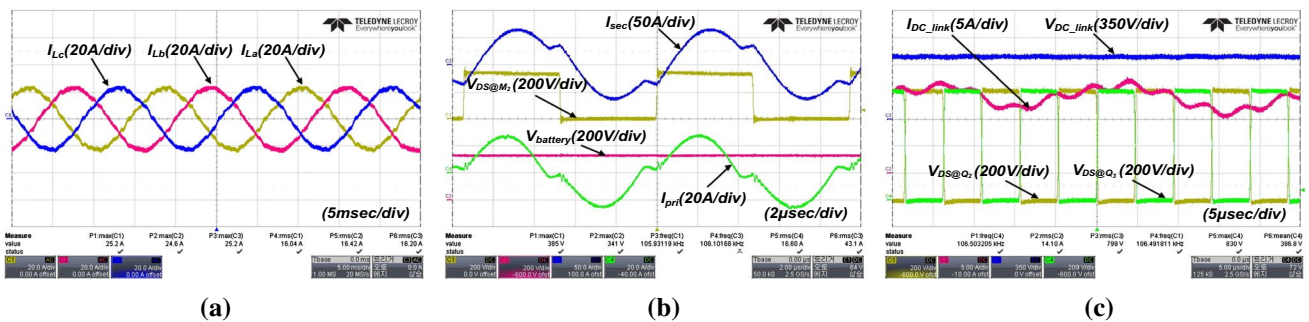


**Fig. 15** Key waveforms in the generation mode with a nominal battery voltage of 330 V: **a** output currents; **b** resonant currents, secondary switch voltage, and battery voltage; **c** DC-link current, DC-link voltage, and primary switch voltages

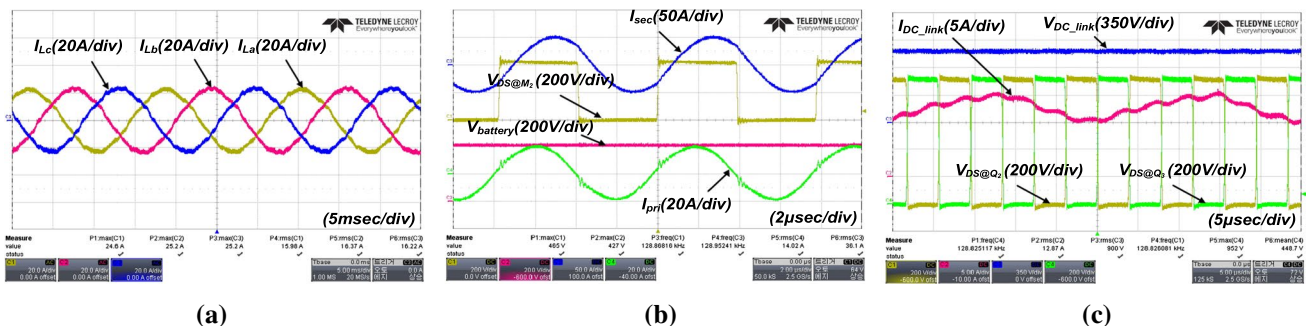


**Fig. 16** Key waveforms in the generation mode with a nominal battery voltage of 413 V: **a** output currents; **b** resonant currents, secondary switch voltage, and battery voltage; **c** DC-link current, DC-link voltage, and primary switch voltages

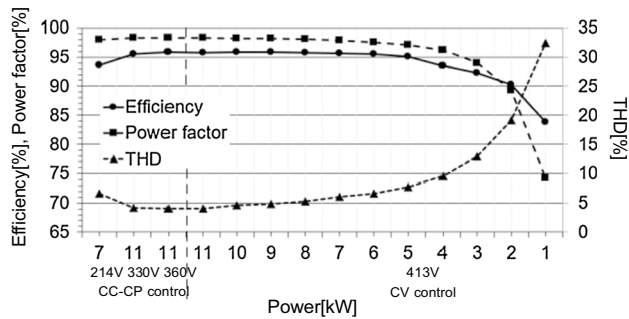


**Fig. 17** Efficiency, power factor, and THD in the charging mode

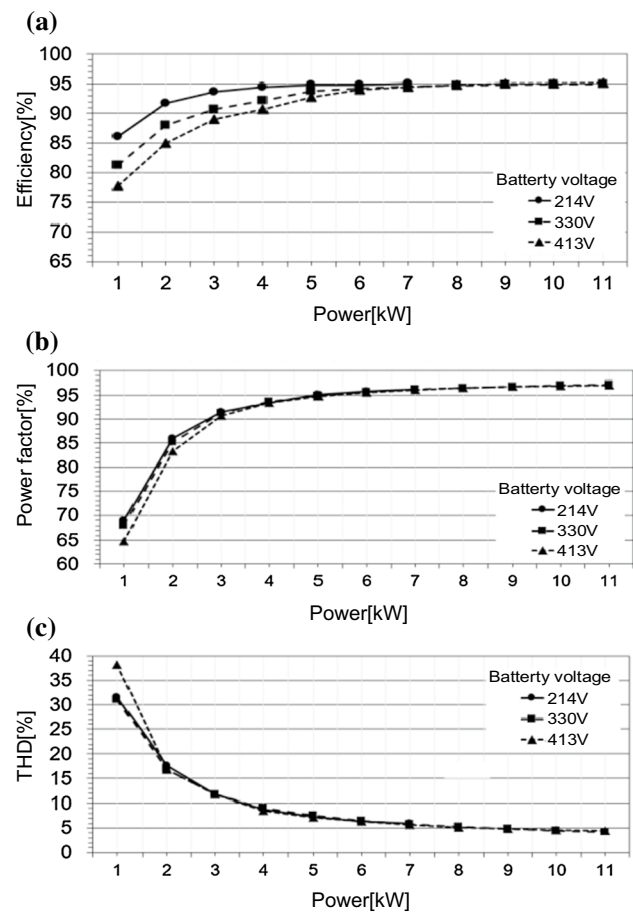
This is due to the secondary-side leakage inductances of the transformers and parasitic stray inductances, which are not visible in the charging mode, and affect the gain of the resonant tanks in the generation mode. Despite slight differences in the operating frequency between the theoretical analysis and the experiments, Figs. 15 and 16 show that all of the voltage gains in the generation mode are achieved and that the ZVS operation in the generation mode is still achieved well by observing the secondary-switch voltage and secondary resonant current waveforms. From all the experimental results in the charging mode and the generation mode, it is confirmed that the proposed OBC prototype operates normally under the maximum load condition of 11 kW.

Figure 17 shows the efficiency, power factor, and total-harmonic distortion (THD) in the charging mode. The prototype OBC achieves efficiencies of up to 96.1%, power factors of up to 98.32%, and THDs of at least 4.09%. Figure 18 shows the efficiency, power factor, and THD in the generation mode. Generation operation is checked individually according to the battery voltage and load conditions. Efficiencies of up to 95.17%, power factors of up to 97.11%, and THDs of at least 4.17% are achieved.

Through testing in the charging mode and in the generation mode, it is confirmed that the proposed OBC prototype has excellent performance in terms of high efficiency, good power factor, and low THD despite the occurrence of changes in battery voltage.

## 9 Conclusion

Recently, the power processing capacity of on-board chargers for electric vehicles has increased to 11 or 22 kW. In addition, chargers with a bi-directional power flow are required since the vehicle-to-load (V2L) and vehicle-to-grid (V2G) markets are rapidly forming. Developing a bi-directional high-capacity EV-mounted charger that can achieve a high-power density while maintaining a high efficiency



**Fig. 18** Generation mode performance according to the battery voltage conditions: **a** efficiency; **b** power factor; **c** THD

over wide battery voltage and load ranges presents a tough technical challenge.

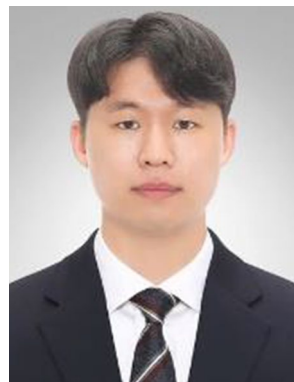
This paper proposes a topology suitable for such a bi-directional EV charger, presents its optimal design, and details a suitable control algorithm implementation. In addition, its system validity is verified by fabricating and experimentally testing an 11 kW prototype. The proposed topology achieves an efficiency of over 95% in both the charging and generation modes with the 11 kW capacity prototype and maintains high-efficiency performance over a wide range of battery voltage conditions. As a result, it can be concluded that the proposed OBC topology shows a great amount of promise and is suitable for bi-directional EV-mounted charger applications.

**Acknowledgements** This research was supported by Korea Electric Power Corporation. (Grant Number: R21XO01-11)



## References

- Ahmad, A., Alam, M.S., Chabaan, R.: A comprehensive review of wireless charging technologies for electric vehicles. *IEEE Trans Transport Electrific* **4**(1), 38–63 (2018)
- Mahone, A., et al.: On the path to Decarbonization: electrification and renewables in California and the Northeast United States. *IEEE Power Energy Mag.* **16**(4), 58–68 (2018)
- Lee, W., Kim, J., Lee, J., Lee, I.: Design of an isolated DC/DC topology with high efficiency of over 97% for EV fast chargers. *IEEE Trans Veh Technol* **68**(12), 11725–11737 (2019)
- Badawy, M.O., Arafat, M.N., Ahmed, A., Anwar, S., Sozer, Y., Yi, P., Abreu-Garcia, J.D.: Design and Implementation of a 75 kW mobile charging system for electric vehicles. *IEEE Trans Ind Appl* **52**(1), 369–377 (2016)
- Lin, W., Hua, C.: Active battery balancing circuit with AC-link technique based on current-fed-push-pull converter, *IEEE*, 339–342 (2017)
- Kumar, B.V., Singh, R.K., Mahanty, R.: A modified non-isolated bidirectional DC-DC converter for EV/HEV's traction drive systems, 2016 IEEE International Conference on Power Electronics, Drives and Energy Systems (PEDES), Trivandrum, 1–6 (2016)
- González, M.A., Escalante, M.F.: Traction system for an EV based on induction motor and 3-level NPC inverter multilevel converters, 12th IEEE International Power Electronics Congress, San Luis Potosi, 73–77 (2010)
- U.S. DRIVE Department of Energy, “Electrical and electronics technical team roadmap,” Oct. 2017. [Online]. Available: <https://www.energy.gov/sites/prod/files/2017/11/f39/EETT%20Roadmap%2010-27-17.pdf>
- Jung, C.: Power Up with 800 V Systems: The benefits of upgrading voltage power for battery-electric passenger vehicles. *IEEE Electrific Mag* **5**(1), 53–58 (2017)
- Porsche Newsroom, “Porsche Taycan - The charging process: Quick, comfortable, intelligent and universal,” Sep. 4, 2019. [Online]. Available: <https://newsroom.porsche.com/en/products/taycan/charging-18558.html>
- Li, B., Jing, L., Wang, X., Chen, N., Liu, B., Chen, M.: A Smooth Mode-Switching Strategy for Bidirectional OBC Base on V2G Technology,” 2019 IEEE Applied Power Electronics Conference and Exposition (APEC), Anaheim, CA, USA, 3320–3324 (2019)
- Kisacikoglu, M.C., Kesler, M., Tolbert, L.M.: Single-phase on-board bidirectional PEV charger for V2G reactive power operation. *IEEE Trans Smart Grid* **6**(2), 767–775 (2015)
- Lee, B., Kim, J., Kim, S., Lee, J.: An isolated/bidirectional PWM resonant converter for V2G(H) EV on-board charger. *IEEE Trans Veh Technol* **66**(9), 7741–7750 (2017)
- Fahem, K., Chariag, D.E., Sbita, L.: On-board bidirectional battery chargers topologies for plug-in hybrid electric vehicles,” 2017 International Conference on Green Energy Conversion Systems (GECS), Hammamet, 2017, 1–6 (2017)
- Khaligh, A., D'Antonio, M.: Global trends in high-power on-board chargers for electric vehicles. *IEEE Trans Veh Technol* **68**(4), 3306–3324 (2019)
- Lu, J., Tian, Q., Bai, K., Brown, A., McAmmond, M.: An indirect matrix converter based 97%-efficiency on-board level 2 battery charger using E-mode GaN HEMTs, 2015 IEEE 3rd Workshop on Wide Bandgap Power Devices and Applications (WiPDA), Blacksburg, VA, 351–358 (2015)
- Monteiro, V., Gonçalves, H., João Afonso, L.: Impact of Electric Vehicles on Power Quality in a Smart Grid Context, 11 th IEEE International Conference on Electrical Power Quality and Utilisation (EPQU), Lisbon, Portugal, 17–19 (2011)
- Greifelt, A., Heiland, G., Gerling, D.: Modular 11kW bidirectional onboard charger with SiC-MOSFET technology for mobile applications, 2017 Brazilian Power Electronics Conference (COBEP), Juiz de Fora, 1–6 (2017)
- Li, B., Li, Q., Lee, F.C., Liu, Z., Yang, Y.: A high-efficiency high-density wide-bandgap device-based bidirectional on-board charger. *IEEE J Emerg Sel Topics Power Electron* **6**(3), 1627–1636 (2018)
- Huang, X., Liu, Z., Li, Q., Lee, F.C.: Evaluation and application of 600 V GaN HEMT in cascode structure. *IEEE Trans Power Electron* **29**, 2453–2461 (2014)
- Whitaker, B., Barkley, A., Cole, Z., Passmore, B., Martin, D., McNutt, T.R., et al.: A high-density, high-efficiency, isolated on-board vehicle battery charger utilizing silicon carbide power devices. *IEEE Trans Power Electron* **29**, 2606–2617 (2014)
- Chang, H., Liang, T., Yang, W.: Design and Implementation of Bidirectional DC-DC CLLC Resonant Converter, 2018 IEEE Energy Conversion Congress and Exposition (ECCE), Portland, OR, USA, 2712–2719 (2018)
- Jung, J., Kim, H., Ryu, M., Baek, J.: Design methodology of bidirectional CLLC resonant converter for high-frequency isolation of DC distribution systems. *IEEE Trans Power Electron.* **28**(4), 1741–1755 (2013)
- Garinto, D., Sutikno, T.: Three-Phase AC-DC Converter with Asymmetrical Vienna Rectifier, 2019 IEEE Conference on Energy Conversion (CENCON), Yogyakarta, Indonesia, 177–181 (2019)
- Vazquez, S., et al.: Optimized Direct Power Control Strategy using Output Regulation Subspaces and Pulse Width Modulation, IECON 2006—32nd Annual Conference on IEEE Industrial Electronics, Paris, France, 1896–1901 (2006)
- Zhang, Y., Peng, Y.: Model predictive current control with optimal duty cycle for three-phase grid-connected AC/DC converters,” 2014 International Power Electronics and Application Conference and Exposition, Shanghai, China, 837–842 (2014)
- Lim, C., Jeong, Y., Moon, G.: Phase-shifted full-bridge DC–DC converter with high efficiency and high power density using center-tapped clamp circuit for battery charging in electric vehicles. *IEEE Trans Power Electron* **34**(11), 10945–10959 (2019)
- Qu, L., Wang, X., Zhang, D., Bai Z., Liu, Y.: A High Efficiency and Low Shutdown Current Bidirectional DC-DC CLLC Resonant Converter, 2019 22nd International Conference on Electrical Machines and Systems (ICEMS), Harbin, China, 1–6 (2019)
- Deng, J., Li, S., Hu, S., Mi, C.C., Ma, R.: Design methodology of LLC resonant converters for electric vehicle battery chargers. *IEEE Trans Veh Technol* **63**(4), 1581–1592 (2014)



**Sang-Youn Lee** received his B.S. and M.S. degrees in Electrical Engineering from Myongji University, Yongin, South Korea, in 2019 and 2021, respectively. His current research interests include battery chargers for EVs and high-power DC-to-DC converters.





**Woo-Seok Lee** received his B.S. and M.S. degrees in Electronics Engineering from Keimyung University, Daegu, South Korea, in 2015 and 2017, respectively. He is presently working towards his Ph.D. degree at Myongji University, Yongin, South Korea. His current research interests include high efficiency and high power-density battery chargers for electric vehicles and digital control.



**Jun-Young Lee** received his B.S. degree in Electrical Engineering from Korea University, Seoul, South Korea, in 1993; and his M.S. and Ph.D. degrees in Electrical Engineering from the Korea Advanced Institute of Science and Technology (KAIST), Daejeon, South Korea, in 1996 and 2001, respectively. From 2001 to 2005, he was a Manager with Plasma Display Panel Development Group, Samsung SDI, Cheonan, South Korea, where he was involved in circuit and product development. From

2005 to 2008, he was a Faculty Member in the School of Electronics and Computer Engineering, Dankook University, Cheonan, South Korea. In 2008, he joined the Department of Electrical Engineering, Myongji University, Yongin, South Korea, as an Associate Professor. His current research interests include power electronics, converter

topology design, soft-switching techniques, display driving systems, and battery charger systems. Dr. Lee is a member of the Korea Institute of Electrical Engineering, the Korea Institute of Power Electronics, the IEEE Industrial Electronics Society, and the IEEE Power Electronics Society.



**Il-Oun Lee** received his B.S. degree in Electrical and Electronic Engineering from Kyungpook National University, Daegu, South Korea, in 2000; his M.S. degree in Electrical Engineering from Seoul National University, Seoul, South Korea, in 2002; and his Ph.D. degree from the Korea Advanced Institute of Science and Technology (KAIST), Daejeon, South Korea, in 2013. From 2003 to 2008, he was a Manager with the Plasma Display Panel Development Group, Samsung SDI, Cheonan,

South Korea. From 2008 to 2013, he was a Senior Engineer in the Power Advanced Development Group, Samsung Electro-Mechanics Co., Ltd., Suwon, South Korea. From 2013 to 2015, he was a Senior Researcher in the Energy Saving Lab., Korea Institute of Energy Research (KIER), Daejeon, South Korea. From 2015 to 2017, he was an Associate Professor in the School of Electrical and Electronics Engineering, Keimyung University, Daegu, South Korea. In 2017, he joined the Department of Electrical Engineering, Myongji University, Yongin, South Korea, as an Associate Professor. His current research interests include DC-DC converters, power factor correction (PFC) AC-DC converters, LED drivers, battery chargers for electric vehicles, digital display power systems, and digital control approaches for DC-DC converters. Dr. Lee is a member of the Korea Institute of Power Electronics, the IEEE Industrial Electronics Society, and the IEEE Power Electronics Society.